nature photonics

SUPPLEMENTARY INFORMATION

DOI: 10.1038/NPHOTON.2014.138

Supplementary Information

Integrated flexible chalcogenide glass photonic devices

Lan Li[1†], Hongtao Lin[1†], Shutao Qiao[2†], Yi Zou[1], Sylvain Danto[3], Kathleen Richardson[3, 4], J. David Musgraves[4], Nanshu Lu[2], and Juejun Hu[1*]

1. Department of Materials Science and Engineering

University of Delaware

Newark, Delaware 19716

2. Centre for Mechanics of Solids, Structures and Materials

Department of Aerospace Engineering and Engineering Mechanics

University of Texas at Austin

Austin, Texas 78712

3. College of Optics and Photonics, CREOL

Department of Materials Science and Engineering

University of Central Florida

Orlando, Florida 32816

4. IRradiance Glass Inc.

Orlando, FL 32828, USA

†These authors contributed equally to this work.

*e-mail: hujuejun@udel.edu

 DOI: 10.1038/NPHOTON.2014.138

In this Supplementary Information, we provide further details on the device fabrication, characterization, and simulation results.

I. Ultra-thin SU-8 planarization tests

II. Propagating loss in $Ge_{23}Sb_7S_{70}$ glass micro-resonators fabricated on flexible substrates and the impact of bending

III. Fatigue test on flexible photonic devices

IV. Measurements of material mechanical and optical properties

V. FEM simulation and analytical modeling accounting for multiple neutral axes in the multilayer stack

VI. *In-situ* strain-optical coupling characterization method

VII. Strain-optical coupling theory

VIII. Optimized 3-D photonic device design parameters

IX. Scattering matrix formalism for calculating the transfer function of vertically coupled add-drop filters

X. Woodpile photonic crystal diffraction experiment configuration

I. Ultra-thin SU-8 planarization tests

Planarization is the key to our multilayer 3-D fabrication process. We choose SU-8, an epoxy-based negative photoresist, as the planarizing agent. Unexposed SU-8 is a thermoplastic with a glass transition temperature (T_g) of 50 °C [1], which is amenable to thermal reflow processing at a relatively low temperature to create a smooth surface finish through the action of surface tension. Once cured or UV cross-linked, SU-8 transforms to a thermosetting polymer with a high T_g > 200 °C and stable thermal/mechanical/chemical properties. To validate the planarization behaviour of SU-8 on glass devices, a layer of 460 nm thick SU-8 epoxy was spin coated on gratings patterned in a 360 nm thick $Ge_{23}Sb_7S_{70}$ film (i.e. 100 nm overcoating layer thickness). Fig. S1a shows top-view optical micrographs of the grating patterns after SU-8 spin coating. The gratings have a fixed duty cycle of 0.5 and their periods are varied from 1.2 μm to 120 μm. The SU-8 layer topography after heat treatment was examined using cross-sectional SEM, and Fig. S1b (bottom) shows an exemplary SEM image of the grating structure after planarization. Transfer function of the planarization process was plotted as a function of spatial frequency (reciprocal of grating pitch) in Fig. S1c. Top panel of Fig. S1b schematically illustrated the definition of degree of planarization (DOP) and planarization angle (θ). The degree of planarization (DOP) is given by: $DOP = 100\% * \frac{t_1 - t_2}{t_2}$, and the planarization angle (θ) by $\theta = \arctan(\frac{t_1 - t_2}{W})$, where W is width of the grating line (i.e. half of the grating pitch). The ultra-thin (100 nm thickness) SU-8 overcoating layer produces DOP consistently larger than 98% for patterns with micron-sized pitch. Such planarization performance is considerably better than previous reports using BCB, PMMA or polyimide as the planarization agent, as shown by the comparison in Table S1.

DOI: 10.1038/NPHOTON.2014.138

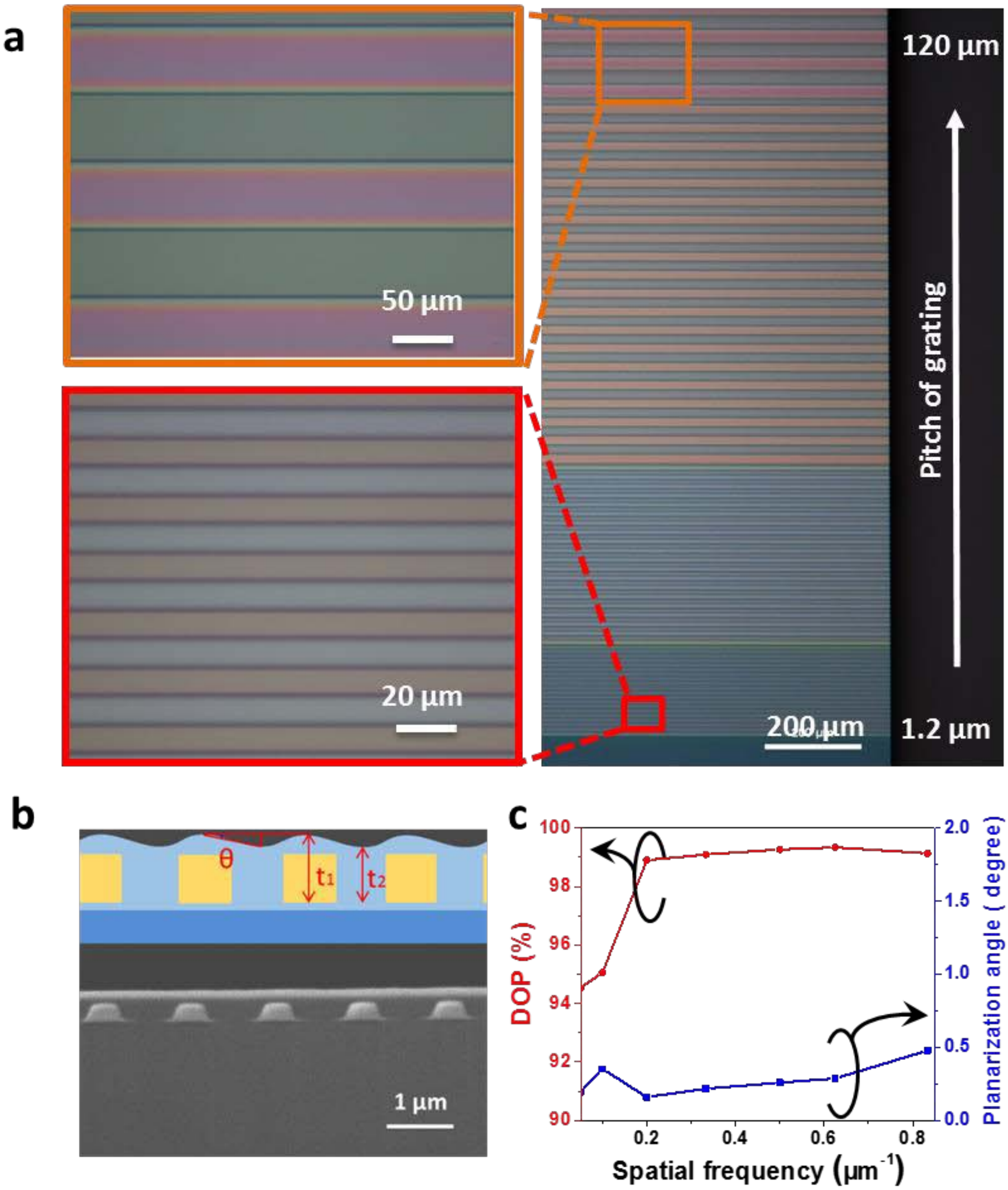

Figure S1 | Ultra-thin SU-8 planarization characterizations. **a**, Optical microscope images of glass grating patterns after single-layer SU-8 planarization. **b**, SEM cross-sectional image of planarized gratings; the top inset illustrates the definition of DOP and planarization angle. **c**, Plot of degree of planarization and planarization angle as functions of spatial frequency. The SU-8 planarization process consistently shows a DOP above 98% over micron-sized features and a small planarization angle < 1°.

Table S1 | Degree of planarization (DOP) of thin SU-8 compared to literature values using Polybenzocyclobutene (PBCB), Poly(methyl methacrylate) (PMMA) and polyimide (PI). The overcoating layer thickness is defined as the thickness of the planarization coating minus that of the underlying features to be planarized.

Materials	Overcoating thickness (µm)	Planarized topography	DOP
SU-8 (this report)	0.1	5 µm pitch grating (duty cycle 0.5)	99%
	0.1	20 µm pitch grating (duty cycle 0.5)	95%
BCB[2]	0.3	10 µm wide trenches on a pitch of 30 µm	90%
	0.3	10 µm wide trenches on a pitch of 120 µm	70%
PBCB[3]	4.5	20 µm pitch grating (duty cycle 0.5)	85%
PI2555[3]	1	20 µm pitch grating (duty cycle 0.5)	50%
PMMA[3]	0.5	20 µm pitch grating (duty cycle 0.5)	18%

 DOI: 10.1038/NPHOTON.2014.138

II. Propagating loss in $Ge_{23}Sb_7S_{70}$ glass micro-resonators fabricated on flexible substrates and the impact of bending

Since the flexible substrates are not amenable to cleavage, it is difficult to use the cut-back method to measure waveguide propagating loss. The non-planar nature of the devices also makes scattered light streak imaging unreliable. Therefore, we choose to evaluate the propagation loss in the flexible photonic devices using optical resonator measurements. The linear propagation loss α in a traveling-wave optical resonator is related to its intrinsic Q-factor Q_{in} through:

$$\alpha = 2\pi n_g / Q_{in}\lambda \tag{S1}$$

where n_g denotes the group index of the resonant mode and λ is the resonant wavelength. The intrinsic quality factor can be deduced from the loaded Q-factor and resonant peak extinction ratio following protocols outlined in literature[4]. This method is particular suitable for flexible device characterization as it directly probes the modal attenuation in resonators and does not require reproducible facet quality. It is worth noting that since we used micro-disk resonators in our experiments, the loss figures cited in this section refer to the linear propagation loss of micro-disk modes.

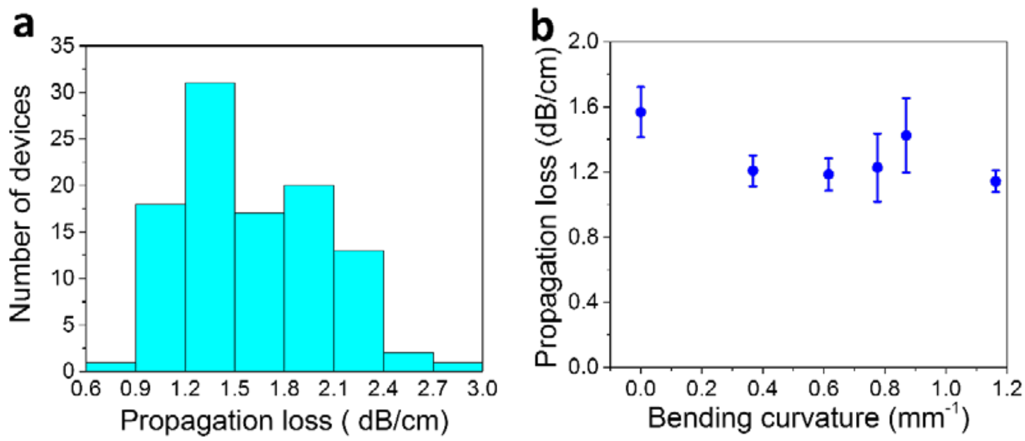

Figure S2 | Propagation loss in flexible optical resonators. **a**, Optical loss distribution measured in flexible micro-disk resonators. **b**, Optical loss in a flexible resonator as a function of bending radius measured when the device was in the mechanically deformed state.

The statistical distribution of propagation loss in the resonator devices we measured is presented in Fig. S2a (calculated from Fig. 1e). The average loss is (1.6 ± 0.4) dB/cm. Our prior measurement showed that the intrinsic material loss in thermally evaporated $Ge_{23}Sb_7S_{70}$ films was well below 0.5 dB/cm[5], and thus sidewall roughness scattering is the primary loss mechanism in our devices. We further note that optical loss in the devices is largely independent of the bending radius when they are mechanically deformed: as an example, Fig. S2b plots the propagation loss in a flexible resonator measured when the device was bent. The change imparted by the bending deformation is insignificant considering the measurement error. This observation can be readily explained by the tight optical confinement in our high-index-contrast photonic devices, which effectively suppresses radiative loss in bent guided wave structures. Fig. S3b shows the quasi-TE mode radiative loss due to bending in a $Ge_{23}Sb_7S_{70}$ waveguide of 800 nm width and 450 nm height, simulated using the full-vectorial waveguide mode solver package FIMMWAVE (Photon Design). It is apparent that radiative bending loss remains negligible down to 50 μm radius. Therefore, it is anticipated that no radiative loss was experimentally observed when we mechanically deform our flexible chip.

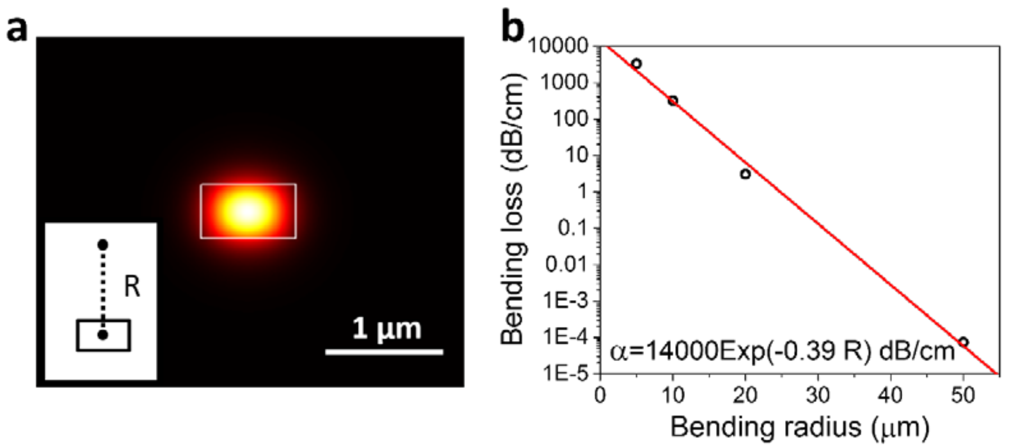

Figure S3 | Bending loss simulations. **a,** Quasi-TE mode intensity profile for a 0.8 μm × 0.45 μm waveguide with a bending radius of 500 μm; the inset illustrates the waveguide bending direction in our mechanical tests. **b**, Radiative bending losses at different bending radii fitted to an exponential model.

 DOI: 10.1038/NPHOTON.2014.138

III. Fatigue test on flexible photonic devices

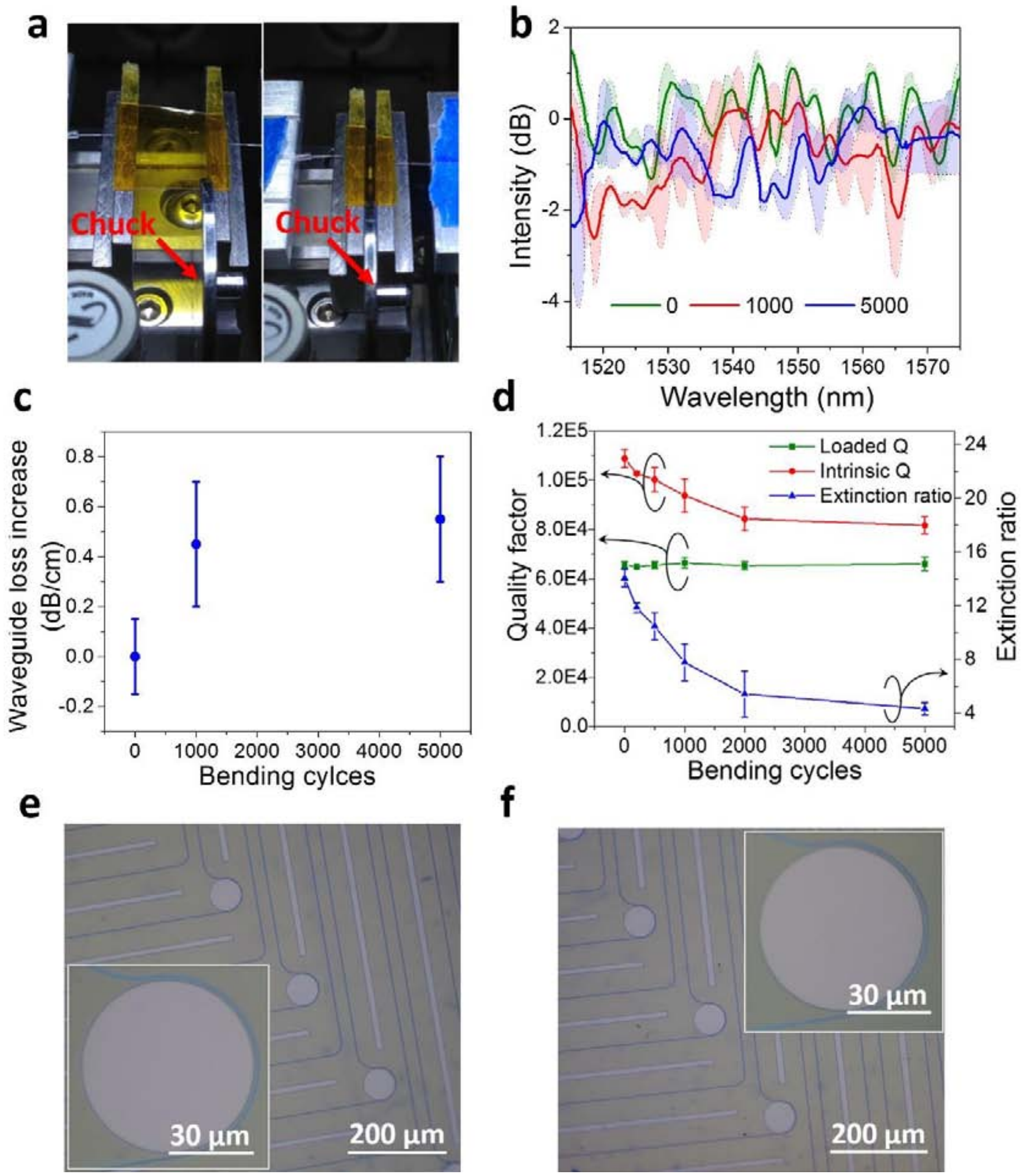

Figure S4 | Fatigue test of the flexible photonic chip. **a**, Photos of the fatigue testing setup. The red arrow points to the metal chuck spacer. **b**, Normalized optical transmission spectra of a flexible waveguide after multiple bending cycles at 0.8 mm bending radius. The shaded regions denote the measurement error bar, which was defined as the standard deviation of optical transmittance collected in multiple transmission measurements. **c**, Spectrum-averaged (1510-1580 nm wavelengths) waveguide propagation loss change due to repeated bending cycles. **d**, Loaded Q-factors, intrinsic Q-factors and extinction ratios of a flexible $Ge_{23}Sb_7S_{70}$ micro-disk resonator after multiple bending cycles at 0.8 mm bending radius. **e**, Top-view optical microscope image of flexible resonators prior to the fatigue test. **f**, Optical microscope image of the same set of resonators after 5,000 bending cycles at 0.8 mm bending radius, revealing structural integrity of the devices free of cracks. The scattered spots are dust particles deposited on the chip surface during the mechanical tests, which were carried out in a non-cleanroom environment.

Fatigue tests of flexible electronic or optoelectronic devices evaluate the mechanical durability of the devices as they undergo repetitive bending for a large number (> 1,000) of cycles. Fig. S4a shows the experimental setup we used for the fatigue test. Two edges of a flexible chip was attached to two sample holders, and the holders were mounted on a sliding track. Linear translational motion of the holders thus resulted in bending of the chip. To reproducibly control the bending radius, metal chucks of different thicknesses were glued to one of the holders as spacers to define the translational distance and hence bending radius. Optical transmission spectra of waveguides and resonators were repeatedly measured in a “flat” state of the chip using fiber end-fire coupling before and after multiple bending cycles at 0.8 mm bending radius. It is worth pointing out that the flexible chip we used for the fatigue tests was a different one from the sample used to obtain the data in Fig. 1f.

Fig. S4b plots the insertion loss of a flexible $Ge_{23}Sb_7S_{70}$ waveguide before and after up to 5,000 bending cycles: the same waveguide was used throughout the measurement to ensure consistent facet quality. The intensity fluctuations were partially attributed to excitation of higher order modes at the 2 μm wide input/output waveguide taper sections. The changes of waveguide propagation loss deduced from the measurement were plotted in Fig. S4c. The results indicate a (0.5 ± 0.3) dB/cm waveguide loss increase after 5,000 cycles at a frequency of 1.5 Hz. The same fatigue tests were performed on $Ge_{23}Sb_7S_{70}$ micro-disk resonators. After 5,000 bending cycles, we observed a 23% decrease of the device intrinsic Q-factor. We inspected the flexible chip under optical microscope (up to 50x magnification) before and after 5,000 bending cycles and no micro-cracks were observed across the chip. Therefore, we conclude that the loss increase (~ 0.5 dB/cm) likely stems from layer delamination or sub-micron cracks that cannot be resolved with an optical microscope, although further study is required to elucidate the loss mechanism. The superior mechanical durability of our devices can be seen from a comparison with state-of-the-art flexible

 DOI: 10.1038/NPHOTON.2014.138

electronic devices shown in Table S2. To the best of our knowledge, our study also represents the first report of fatigue analysis on flexible micro-electronic or micro-photonic devices that can sustain sub-millimetre bending.

Table S2 | Summary of reported fatigue testing results of flexible micro-electronic and photonic devices.

Device type	Bending radius (mm)	Bending cycles	Performance metric	Percentage change after tests
Chalcogenide glass resonator (this report)	0.8	5000	Quality factor	23%
OLED with transparent contacts[1]	10.5	1000	Electroluminesence intensity	50%
PDMS flat-panel solar cell concentrator[2]	20	1000	Efficiency	Insignificant
Flexible molecular-scale electronics[3]	5	1000	Decay coefficient	17%
Flexible a-IGZO TFT amplifier[4]	5	1000	Gain	Insignificant
Flexible grapheme based capacitor[5]	5	10000	Capacitance	3.5%
Flexible silicon thin film transistor[6]	3	2000	Threshold voltage	< 20%

IV. Measurements of material mechanical and optical properties

The Young's moduli of the constituent materials were experimentally extracted from uniaxial tensile tests performed on an RSA3 dynamic mechanical analyser (TA instruments) with a Hencky strain rate of 0.01 s^{-1}. The layer thicknesses were measured by optical microscopy (Fig. S5a). The uniaxial strain-stress characteristics of the silicone adhesive layer and the polyimide layer were measured on the Kapton tapes. Specifically, two sets of experiments were performed: a double-layer Kapton tape was stretched in-plane to determine the modulus of polyimide, and a stack of Kapton tapes (Fig. S5a) underwent out-of-plane tensile tests to extract the strain-stress behaviour of the silicone adhesive layer. In the former case, since the modulus of polyimide is over three orders of magnitude higher than that of silicone, the in-plane stress is pre-dominantly sustained by the polyimide layer. In the latter case, the strain primarily occurred in the silicone layer given its much lower modulus. The two measurements are analogous to the parallel and series connection of two elastic springs with vastly different spring constants (inset of Fig. S5a). Both types of experiments were repeated on multiple (> 6) samples for statistical averaging. The statistically averaged strain-stress curves of polyimide and silicone calculated from the measurement results are plotted in Fig. S5b-c.

In addition to elastic moduli, the strain-optical coefficients are also essential parameters for calculating the strain-optical coupling strength in the flexible resonators, as suggested by Eq. 1. However, measuring strain-optical coefficients, in particular those of thin films (which can be significantly different from those of bulk amorphous glasses), was regarded as extremely challenging task. Here we leverage the flexible resonator devices as a new measurement platform for accurate quantification of strain-optical coefficients of thin film materials. For resonators made of the same material and of the identical dimensions, Eq. 1 suggests the same $d\lambda/d\varepsilon$ coefficient regardless of the flexible device configuration. This conclusion is supported by our experimental results: if we re-plot the strain-induced resonant wavelength shift data (Fig. 2a) as a function of local strain at the resonators, it is clear that all data points fall on a single straight line (Fig. 2b), indicating the same $d\lambda/d\varepsilon$ coefficient (i.e. slope of the line). Since the second and third terms in Eq. 1 (resonator geometry change) can be readily inferred from mechanical simulations, the material strain-optical response can be calculated by subtracting the contributions from the two terms. The calculation was used to generate the theoretical results in Fig. 2a.

DOI: 10.1038/NPHOTON.2014.138

Table S3 | Materials parameters used in our FEM simulations

Materials	Young's Modulus (MPa)	Density (g/cc)	Poisson ratio
Polyimide	Fig. S3b	1.42	0.34
Silicone	Fig. S3c	0.97	0.49
SU-8	2000	1.12	0.22

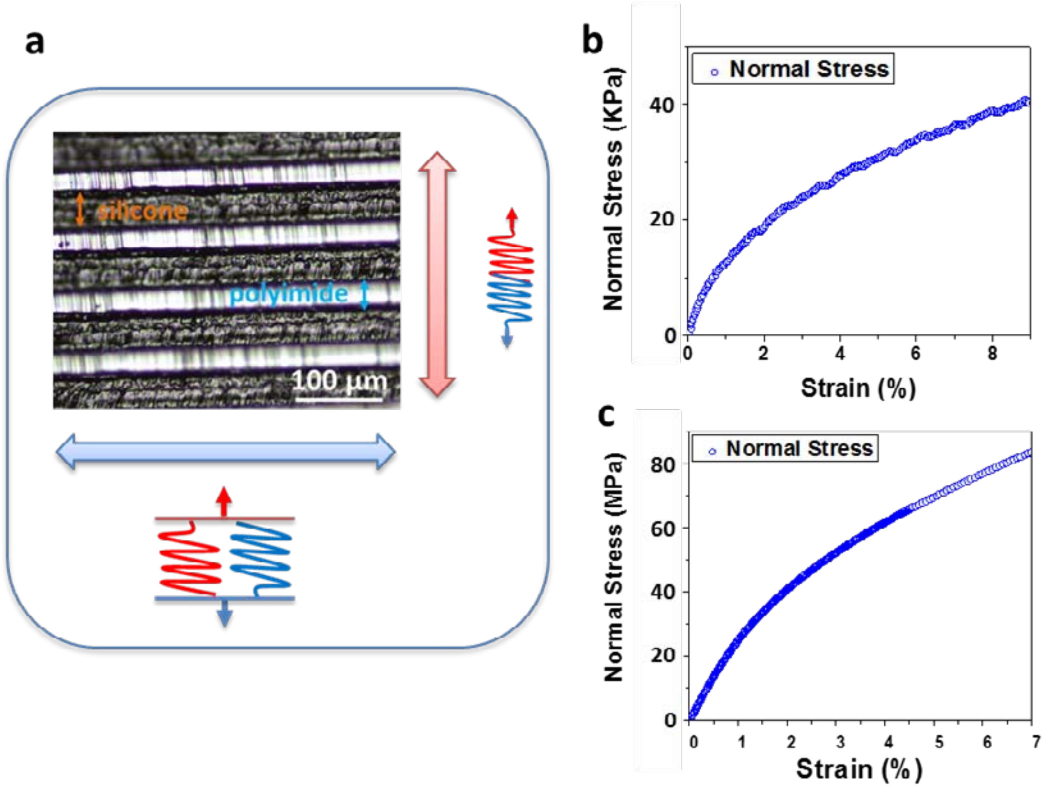

Figure S5 | Mechanical tests of materials used in the flexible photonic device fabrication. a, Cross-sectional optical microscope image of a Kapton tape stack. **b**, Typical stress-strain curve of the silicone layer. **c**, Typical stress-strain curve of the polyimide layer.

V. FEM simulation and analytical modelling accounting for multiple neutral axes in the multilayer stack

When a multilayer structure is subject to pure bending, cross-sectional planes before bending are assumed to remain planar after bending in the classical bending theory. Under this assumption, a unique neutral axis of the laminated structure characterized by the distance *b* from the top surface of PI can be written as:

$$b = \frac{\sum_{i=1}^{3} \overline{E}_i h_i \left[\left(\sum_{j=1}^{i} h_j \right) - \frac{h_i}{2} \right]}{\sum_{i=1}^{3} \overline{E}_i h_i} \tag{S2}$$

where $\overline{E}_i = E_i / \left(1 - \nu_i^2\right)$ represents the plane strain Young's modulus with ν_i being the Poisson's ratio. Bending-induced tensile strain can be calculated analytically using:

$$\varepsilon = \frac{y}{\rho} \tag{S3}$$

where *y* is the distance from the point of interest to the neutral axis and ρ represents the radius of the neutral axis. Strain along the neutral axis is exactly zero and strains on different sides of the neutral axis have opposite signs.

Eq. S2 is only applicable to multilayer stacks with similar elastic stiffness. In our design, the PI and SU-8 layers are much stiffer than the silicon adhesive layer and thus Eq. S2 no longer applies. Fig. S6b shows the strain distribution in a bent flexible photonic chip simulated using FEM: when the multilayer is subject to concave bending, FEM results clearly show that the strain distribution is not monotonic across the stack thickness. Both compressive and tensile strains are present in the PI and SU-8 layers, which is contradictory to Eq. S2 where only one neutral axis exists in the structure.

DOI: 10.1038/NPHOTON.2014.138

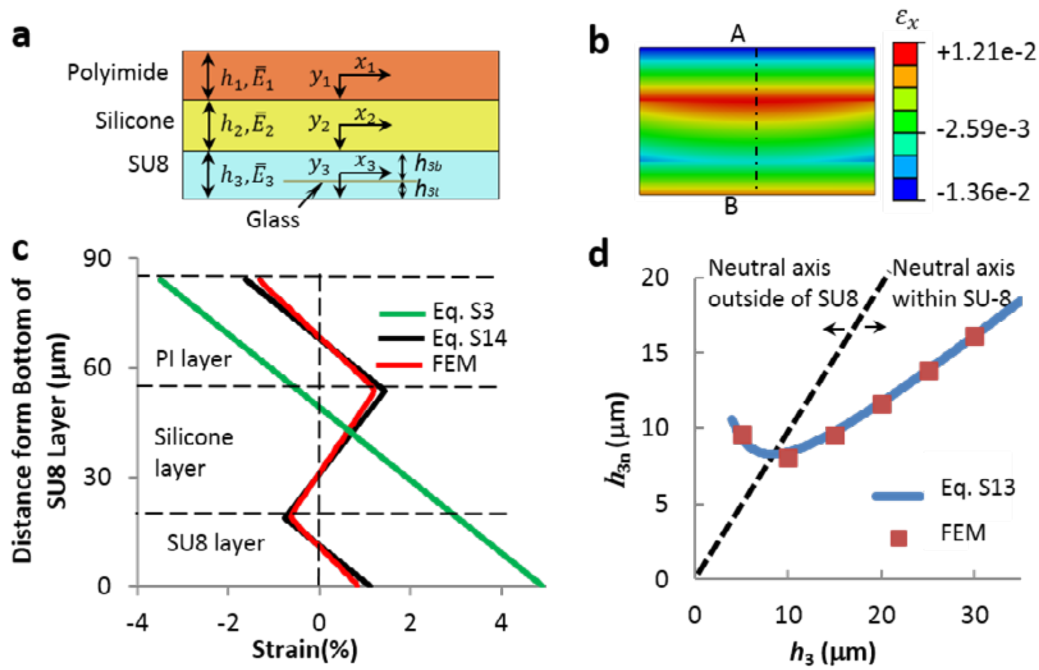

Figure S6 | Multi-neutral-axis theory. **a**, Cross-sectional schematic of the flexible photonic chip, with a PI-silicone-SU8 three-layer structure (not drawn to scale), thickness and plane strain Young's modulus are as labelled, and the local coordinate originates from the median plane of each layer. **b**, Contour plot of bending strain distribution obtained from FEM when the structure in Fig. S6a is bent. **c**, Through-stack strain distribution in the flexible chip with an SU-8 layer thickness of 18.9 µm when bent to a radius of 1 mm: the green line represents results calculated using the conventional theory (Eq. S3), the black curve is derived using our multiple neutral-axes theory (Eq. S14), and the red curve are FEM simulations. **d**, the position of SU-8 neutral axis from SU-8 surface as a function of SU-8 thickness. The blue curve comes from Eq. S13 and the solid markers are FEM results. Dash line denotes the boundary of SU-8. When the h_3 is smaller than the critical value of 8.28 µm, the neutral axis will shift outside SU-8 to the left hand side of the dash line and hence is not accessible to the device.

To accurately predict the strain distribution in each layer, we assume that the cross-sectional planes in PI and those in SU-8 remain planar during bending. Therefore, linear relation between strain and curvature (Eq. S3) is still valid.

The coordinate system we adopt is depicted in Fig. S6a, with notations given in Table S4.

Table S4 | Notations used in the mechanical modelling

Layer	Young's Modulus	Thickness	Strain distribution	Distance from neutral axis to median plane	Distance from neutral axis to bending centre
PI	$\bar{E}_1$	h_1	$\epsilon_1(y_1)$	d_1	ρ_1
silicone	$\bar{E}_2$	h_2	$\epsilon_2(y_2)$	--	--
SU-8	$\bar{E}_3$	h_3	$\epsilon_3(y_3)$	d_3	ρ_3

Our goal is to find an analytical solution for d_3 so that we know where to place the photonic devices for minimum strain.

Using the local coordinate systems, strain in PI can be written as:

$$\epsilon_1(y_1) = \frac{y_1 - d_1}{\rho_1} \; \left(-\frac{h_1}{2} < y_1 < \frac{h_1}{2}\right) \tag{S4}$$

Strain in the SU-8 layer is

$$\epsilon_3(y_3) = \frac{y_3 - d_3}{\rho_3} \; \left(-\frac{h_3}{2} < y_3 < \frac{h_3}{2}\right) \tag{S5}$$

We suppose that strain in silicone layer is a linear function of y_2 as inspired by our FEM results:

$$\epsilon_2(y_2) = a y_2 + b \; \left(-\frac{h_2}{2} < y_2 < \frac{h_2}{2}\right) \tag{S6}$$

where *a* and *b* are coefficients to be determined by continuity conditions at PI/silicone and silicone/SU-8 interfaces.

Continuity at layer interfaces imposes:

$$\begin{cases} \epsilon_2\left(-\frac{h_2}{2}\right) = \epsilon_1\left(\frac{h_1}{2}\right) \\ \epsilon_2\left(\frac{h_2}{2}\right) = \epsilon_3\left(-\frac{h_3}{2}\right) \end{cases} \tag{S7}$$

Force equilibrium in *x* direction imposes:

$$\bar{E}_1 \int_{-\frac{h_1}{2}}^{\frac{h_1}{2}} \frac{y_1 - d_1}{\rho_1} dy + \bar{E}_3 \int_{-\frac{h_3}{2}}^{\frac{h_3}{2}} \frac{y_3 - d_3}{\rho_3} dy_3 + \bar{E}_2 \int_{-\frac{h_2}{2}}^{\frac{h_2}{2}} (a y_2 + b) dy_2 = 0 \qquad \text{(S8),}$$

Combing Eqs. S7 and S8 yields a relation between d_1 and d_3:

$$2\left(\frac{\bar{E}_1 h_1 d_1}{\rho_1} + \frac{\bar{E}_3 h_3 d_3}{\rho_3}\right) = \bar{E}_2 h_2 \left(\frac{\frac{h_1}{2} - d_1}{\rho_1} - \frac{\frac{h_3}{2} + d_3}{\rho_3}\right) \tag{S9}$$

which satisfies the following two extreme cases: (i) When E_2=0, i.e. there is no material layer between PI and SU-8, both d_1 and d_3 should go to zero. (ii) When $\bar{E}_1 = \bar{E}_2 = \bar{E}_3$, i.e. the composite beam decays to a beam of uniform material, there should be only one neutral axis, i.e. $d_1 = \frac{h_2 + h_3}{2}$ and $d_3 = -\frac{h_1 + h_2}{2}$.

Assuming PI and SU-8 have the same original length and the same bending angle, the

 DOI: 10.1038/NPHOTON.2014.138

bending radius from each layer's neutral axis to its bending centre should also be the same, which means

$$\rho_1 = \rho_3 \tag{S10}$$

Substituting Eq. S10 into Eq. S9 yields:

$$2(\bar{E}_1 h_1 d_1 + \bar{E}_3 h_3 d_3) = \bar{E}_2 h_2 \left((\tfrac{h_1}{2} - d_1) - (\tfrac{h_3}{2} + d_3) \right) \tag{S11}$$

As shown in Table S4, $\bar{E}_2 \ll \bar{E}_1$ and $\bar{E}_2 \ll \bar{E}_3$, which implies that the right hand side of Eq. S11 is much smaller than the left hand side and can be approximated as zero, hence

$$d_3 = -d_1 \frac{\bar{E}_1 h_1}{\bar{E}_3 h_3} \tag{S12}$$

For a constant PI thickness, our FEM results have validated a hypothesis that due to the soft silicone interlayer, the thickness of SU-8 has little effect on the position of the neutral axis of PI layer as long as SU-8 is thinner or of comparable thickness to the PI. We may then take d_1 as a constant and by fitting the FEM results, we obtain $d_1 = 0.836\ \mu\text{m}$.

The distance from SU-8 surface to SU-8 neutral axis h_{3n} is thus given by:

$$h_{3\text{n}} = \frac{h_3}{2} + d_1 \frac{\bar{E}_1 h_1}{\bar{E}_3 h_3} \tag{S13}$$

where d_1 = 0.836 μm is the distance from the PI neutral axis to the PI median plane, which is found to be a constant when silicone thickness is fixed. In a single free-standing SU-8 layer, $h_{3\text{n}} = h_3/2$. When SU-8 is bonded to PI via silicone adhesive, the effect of PI is captured by the second term in Eq. S13: the thicker the PI layer (i.e. the larger h_1), the further away the neutral axis of SU-8 from its median plane.

Once the neutral axes are determined, strain distribution across the stack thickness is given by

$$\varepsilon = \begin{cases} \frac{y_1 - d_1}{\rho} & \left(-\frac{h_1}{2} \le y_1 < \frac{h_1}{2}\right) \\ \frac{(\frac{h_2}{2} - y_1)(\frac{h_1}{2} - d_1) - (\frac{h_2}{2} + y_1)(\frac{h_3}{2} + d_3)}{\rho h_2} & \left(-\frac{h_2}{2} \le y_2 < \frac{h_2}{2}\right) \\ \frac{y_3 - d_3}{\rho} & \left(-\frac{h_3}{2} \le y_3 \le \frac{h_3}{2}\right) \end{cases} \tag{S14}$$

where ρ represents the average radius of the multilayer. Results from the conventional bending theory (Eq. S3), FEM, and our new multi-neutral-axis model (Eq. S14) are compared in Fig. S6c. Conventional bending theory predicts monotonic linear strain distribution whereas both FEM and Eq. S14 capture non-monotonic strain distribution in the multilayer stack. Linear strain distribution in each layer obtained from FEM further corroborates our basic assumptions. The locations of zero strain plane for different SU-8 thicknesses calculated using Eq. S13 are plotted in Fig. S6d. The dashed curve in Fig. S6d represents the equation $h_{3\mathrm{n}} = h_3$. When $h_3 < 8.28$ μm, the neutral axis will locate outside the SU-8 layer and hence no longer accessible for device placement.

DOI: 10.1038/NPHOTON.2014.138

VI. *In*-situ strain-optical coupling characterization method

Fig. S7a schematically illustrates the flexible chip testing setup. To facilitate optical coupling into the single-mode waveguides, the 0.8 μm wide bus waveguides are tapered to a width of 2 μm near their end facets. The fibre-to-waveguide coupling loss is not optimized in this work and is estimated to be approximately 4 dB per facet. Fig. S7b shows a far-field image of quasi-TE guided mode output from a single-mode $Ge_{23}Sb_7S_{70}$ glass waveguide on a plastic substrate and Fig. S7c shows a photo of a flexible chip under bending test. The chip was glued onto the linear motion sample stages using double-sided sticky tapes. Bending radius of the flexible chip was measured from the image using an imaging processing software (Image J).

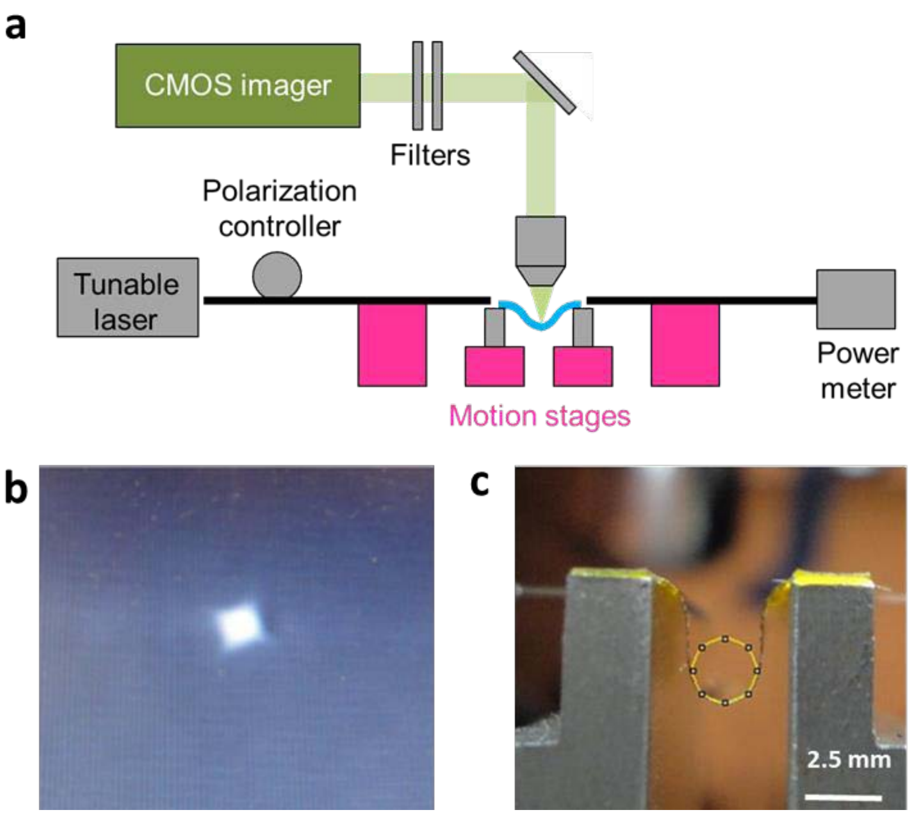

Figure S7 | a, Schematic diagram of the testing setup. **b**, Far-field image of TE guided mode output from a single-mode flexible $Ge_{23}Sb_7S_{70}$ glass waveguide. **c**, Photo of a flexible waveguide chip under bending test: an imaging processing software was used to extract the bending radius of the chip from the image.

VII. Strain-optical coupling theory

This Part of Supplementary Material aims to derive Eq. 1, which governs the strain-optical coupling properties in flexible photonic resonant cavity devices.

The resonant condition of a resonant cavity device can be generally given by:

$$N\lambda = n_{eff}L \tag{S15}$$

when strain introduces a perturbation to the resonant wavelength λ, we have:

$$N(\lambda + d\lambda) = n_{eff}L + d\left(n_{eff}L\right) = n_{eff}L + Ldn_{eff} + n_{eff}dL \tag{S16}$$

The effective index change dn_{eff} originates from two mechanisms: the strain-optical material response, as well as the cross-sectional geometry change of the resonator due to strain:

$$dn_{eff} = \sum_i \Gamma_i \left(\frac{dn}{d\varepsilon}\right)_i d\varepsilon + \frac{dn_{eff}}{d\varepsilon} d\varepsilon + \frac{dn_{eff}}{d\lambda} d\lambda \tag{S17}$$

Here the first term corresponds to the material contribution, and the second term only takes into account the geometric change. The coefficient $dn_{eff}/d\varepsilon$ can be calculated once the local strain at the resonator is known using the perturbation theory involving shifting material boundaries[12]. The third term results from effective index dispersion in the resonator: as the resonant wavelength shifts, the corresponding effective index also changes. Combining the two equations leads to Eq. 1. Note that the group index in Eq. 1 is defined as:

$$dn_{eff} = n_{eff} - d\lambda \frac{dn_{eff}}{d\lambda} \tag{S18}$$

 DOI: 10.1038/NPHOTON.2014.138

VIII. Optimized 3-D photonic device design parameters

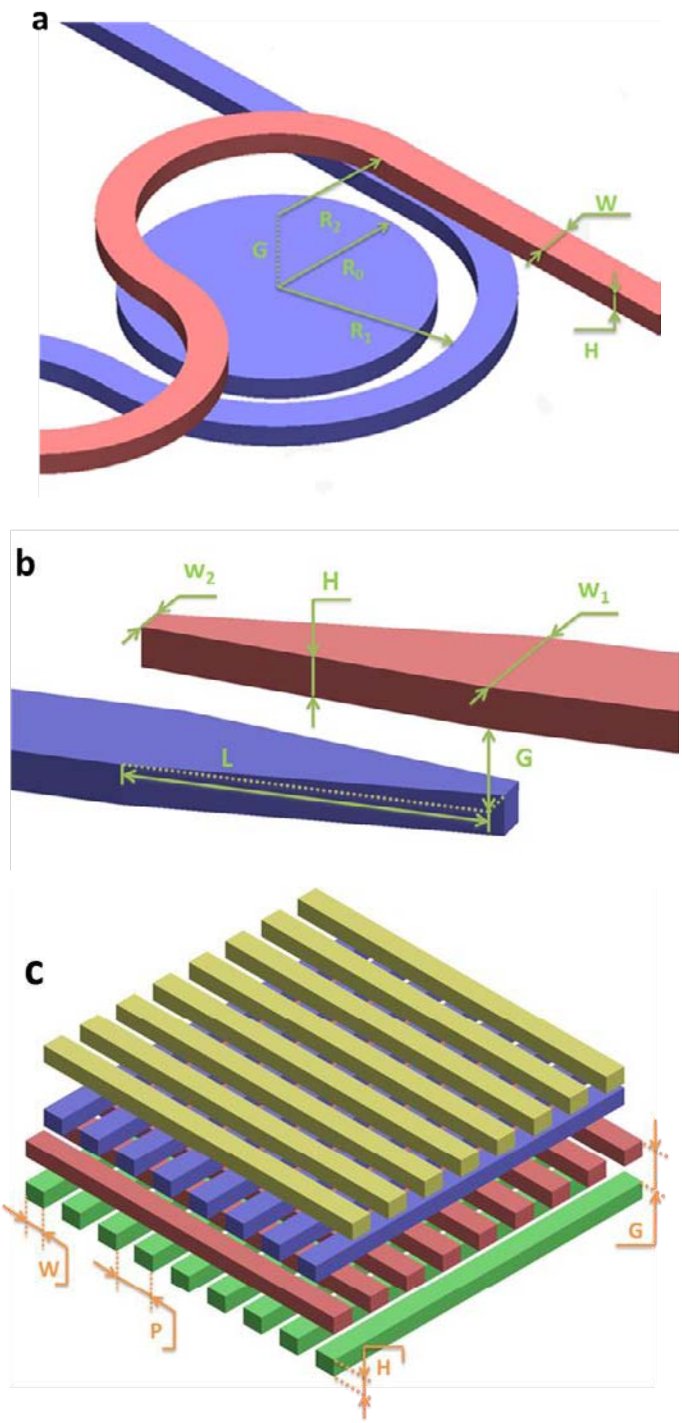

Figure S8 | Schematic structures of 3-D photonic devices. **a**, a two-layer vertically coupled resonator. **b**, An interlayer waveguide couplers. **c**, A woodpile photonic crystal. The key geometric parameters are labelled in the figures.

Table S5 | Optimized 3-D photonic device geometric parameters.

Fig. S8a	W	H	R_0	R_1	R_2	G
(µm)	0.8	0.4	30	30.8	29.4	0.9
Fig. S8b	W_1	W_2	L	H	G	
(µm)	0.9	0.6	40	0.4	0.55	
Fig. S8c	W	P	H	G		
(µm)	1.5	3	0.36	0.8		

A set of 3-D photonic devices with varied design parameters were fabricated and tested. Table S5 summarizes the experimentally determined geometric parameter combinations that yield the optimized performance presented in this study.

 DOI: 10.1038/NPHOTON.2014.138

IX. Scattering matrix formalism for calculating the transfer function of vertically coupled add-drop filters

The vertically coupled add-drop filter can be treated using a circuit model[13] shown in Fig. S9. The power coupling coefficients between the resonator and the add and drop port waveguides are given by K_1 and K_2, respectively. Power loss due to coupling is neglected in the calculation. L is the resonator circumference and α is the optical loss in the micro-disk resonator. Using the scattering matrix method, loaded quality factor Q_{load}, maximum power at the drop port and minimum power at the through port at resonance can be obtained by the equations:

$$Q_{load} = \frac{2\,\pi n_g L}{\lambda_r(K_1+K_2+(1-\sigma^2))} \tag{S19}$$

$$I_{drop-max} = I_{in}\frac{K_1K_2\sigma^2}{(1-\sigma\sqrt{1-K_1}\sqrt{1-K_2})^2} \tag{S20}$$

$$I_{through-min} = I_{in}\frac{(\sqrt{1-K_1}-\sigma\sqrt{1-K_2})^2}{(1-\sigma\sqrt{1-K_1}\sqrt{1-K_2})^2} \tag{S21}$$

where λ is the resonant wavelength, I_{in} is the input power, σ is the intrinsic amplitude loss in one round trip and is expressed as

$$\sigma = \exp(-1/2\ \alpha L) \tag{S22}$$

n_g is the group index of the resonator and can be defined as follows:

$$n_g = c_0/(FSR \cdot L) \tag{S23}$$

Here, c_0 is the light speed in vacuum, and FSR is the free spectral range (FSR) of the resonator in the frequency domain. Based on the measured transmission spectrum (Fig. 4b) and the equations above, the coupling coefficients can be fitted, which in turn allows the prediction of the resonator transmission spectrum. The parameters used in the calculation are listed in Table S6.

The intrinsic quality factor (Q_{in}) of the micro-disk resonator is 1.9×10^5 calculated using[14]

$$Q_{in} = \frac{2\pi n_g}{\alpha\lambda} \tag{S24}$$

which is consistent with that of all-pass resonators we fabricated using the same method.

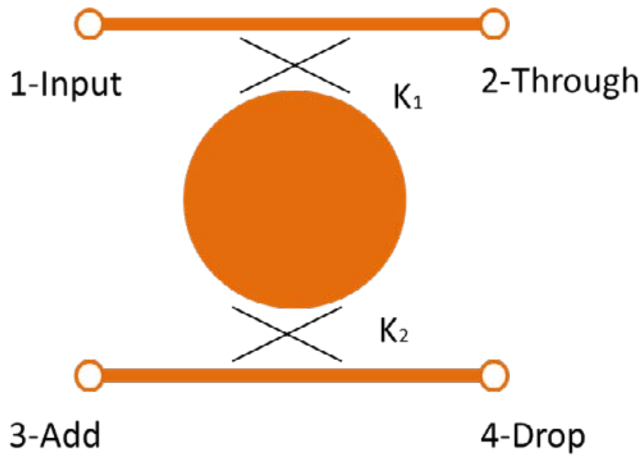

Figure S9 | Schematic illustration of a circuit model of the vertically coupled add/drop filter.

Table S6 | Parameters used to calculate the transmission spectrum of the vertically coupled add/drop resonator filter shown in Fig. 4c.

L(um)	λ_r(nm)	I_{in} (nW)	I_0 (nW)	I_{thmin} (nW)	I_{drmax} (nW)	Q_{load}
188.5	1566.228	87.7	3.2	4.4	67.3	2.2×10^4
FSR(GHZ)	n_g	K_1	K_2	σ	α(dB/cm)	Q_{in}
757	2.10	0.041	0.024	0.996	2.0	1.9×10^5

DOI: 10.1038/NPHOTON.2014.138

X. Woodpile photonic crystal diffraction experiment configurations

Fig. S10 illustrates the diffraction experiment setup. Monochromatic green light from a collimated 532 nm diode-pumped solid state green laser was incident at an angle θ = 45 degrees upon the surface of the PhC sample, and the diffraction patterns were projected onto a white board perpendicular to the (0 0) specular order reflection. To calculate the projected positions of different diffraction orders, the wave vector can be decomposed in the coordinate system shown in Fig. S10, where the x and z axes are in-plane with the woodpile PhC structure while the y axis is perpendicular to the PhC sample surface. For the (0 0) specular order, the wave vector is:

$$\overleftarrow{k}_{(0\,0)} = \left(k_{x0}, k_{y0}, 0\right) = (k_0 cos\theta, k_0 sin\theta, 0) \quad \text{(S25)}$$

where k_0 is the wave vector in vacuum. For a diffraction spot of the (n m) order, its wave vector is:

$$\overleftarrow{k}_{(n\,m)} = \left(k_x, k_y, k_z\right) = (k_{x0} + \mathrm{n}\, G_x, \sqrt{k_0^2 - k_x^2 - k_z^2}, \mathrm{m}\, G_z\ ) \quad \text{(S26)}$$

according to the Bragg diffraction equation, where G_x, G_z are the PhC in-plane reciprocal lattice vectors. Thus the diffraction angle of the (n m) order light with respect to the (0 0) order can be calculated using:

$$\alpha = \arctan\left(\frac{k_x}{k_y}\right) - \theta \quad \text{(S27)}$$

$$\beta = \arctan\left(\frac{k_z}{\sqrt{k_x^2+k_y^2}}\right) \quad \text{(S28)}$$

and the position of the (n m) order pattern in the x'-y' plane (on the white board) is written as:

$$(\mathrm{D}\tan\alpha\ , \mathrm{D}\ \tan\beta\ /\cos\alpha)$$

Diffraction patterns predicted using the approach agree well with the experimental results, as shown in Fig. 5b.

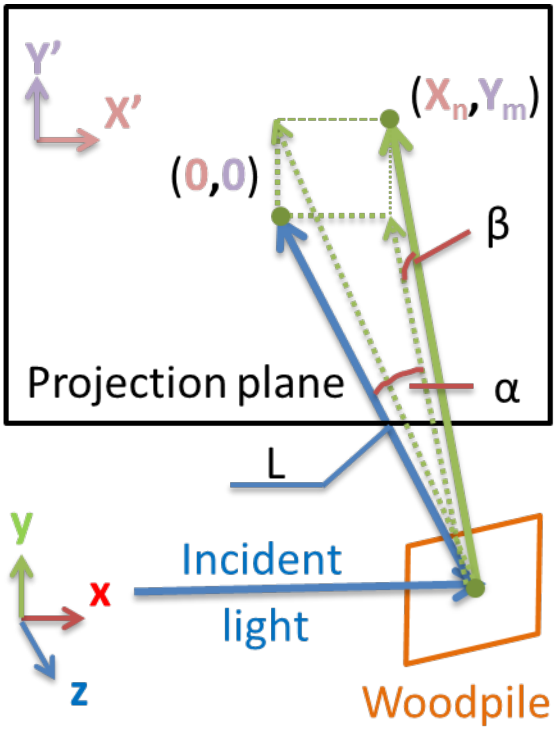

Figure S10 | Schematic diagram illustrating the experimental setup used to map the diffracting patterns from the woodpile photonic crystal structure.

DOI: 10.1038/NPHOTON.2014.138

References:

1. Zhang, Y., Lin, C.T. & Yang, S. Fabrication of Hierarchical Pillar Arrays from Thermoplastic and Photosensitive SU-8. *small* **6**, 768-775 (2010).
2. Roelkens, G. *et al*. Adhesive bonding of InP/InGaAsP dies to processed silicon-on-insulator wafers using DVS-bis-benzocyclobutene. *Journal of the Electrochemical Society* **153**, G1015-G1019 (2006).
3. Schiltz, A. AN EMPIRICAL-MODEL FOR PLANARIZATION WITH POLYMER-SOLUTIONS. *Japanese Journal of Applied Physics Part 1-Regular Papers Short Notes & Review Papers* **34**, 4185-4194 (1995).
4. Xiao, S., Khan, M.H., Shen, H. & Qi, M. Modeling and measurement of losses in silicon-on-insulator resonators and bends. *Optics Express* **15**, 10553-10561 (2007).
5. Hu, J. *et al*. Si-CMOS-compatible lift-off fabrication of low-loss planar chalcogenide waveguides. *Optics Express* **15**, 11798-11807 (2007).
6. Kwak, K., Cho, K. & Kim, S. Stable Bending Performance of Flexible Organic Light-Emitting Diodes Using IZO Anodes. *Scientific Reports* **3**, 2787 (2013).
7. Chou, C.H., Chuang, J.K. & Chen, F.C. High-Performance Flexible Waveguiding Photovoltaics. *Scientific Reports* **3**, 2244 (2013).
8. Park, S. *et al*. Flexible molecular-scale electronic devices. *Nature Nanotechnology* **7**, 438-442 (2012).
9. Munzenrieder, N. *et al*. Flexible a-IGZO TFT amplifier fabricated on a free standing polyimide foil operating at 1.2 MHz while bent to a radius of 5 mm. in *Electron Devices Meeting (IEDM), 2012 IEEE International* 5.2.1-5.2.4 (2012).
10. El-Kady, M.F., Strong, V., Dubin, S. & Kaner, R.B. Laser Scribing of High-Performance and Flexible Graphene-Based Electrochemical Capacitors. *Science* **335**, 1326-1330 (2012).
11. Jong-Hyun, A. *et al*. High-speed mechanically flexible single-crystal silicon thin-film transistors on plastic substrates. *Electron Device Letters, IEEE* **27**, 460-462 (2006).
12. Johnson, S.G. *et al*. Perturbation theory for Maxwell's equations with shifting material boundaries. *Physical Review E* **65** (2002).
13. Schwelb, O. Transmission, group delay, and dispersion in single-ring optical resonators and add/drop filters - A tutorial overview. *Journal of Lightwave Technology* **22**, 1380-1394 (2004).
14. Hu, J. Planar halcogenide glass materials and devices. *Ph.D. thesis* (2009).